Experimental band structure of aluminum

Harry J. Levinson,* F. Greuter, and E. W. Plummer
Department of Physics and Laboratory for Research on the Structure of Matter, University of Pennsylvania, Philadelphia, Pennsylvania 19104-3859
(Received 28 June 1982)

Angle-resolved photoemission utilizing synchrotron radiation as a source was used to measure the occupied and unoccupied band structure of aluminum. The occupied portion of the bands displays a dispersion in qualitative agreement with the nearly-free-electron model and self-consistent band calculations. The measured occupied bandwidth is 10.6 eV, which is 0.5 eV smaller than calculated, due to electron-electron interactions (self-energy). The measured gap at X is 1.68 ± 0.08 eV wide and centered 1.99 ± 0.08 eV below the Fermi energy. The magnitude and position of this gap do not simultaneously agree with any calculation or fit to the Fermi surface. The band structures which are derived by fitting to the Fermi surface or to optical properties reproduce the gap magnitude correctly, but not its position. Band-structure calculations do not reproduce either the gap magnitude or position due to ~0.5-eV discrepancy in the X_1 point. The experimental band structure above the vacuum level is in qualitative agreement with calculations, once inelastic scattering (short mean free path) and evanescent waves from the vacuum solid interface are included. The lifetime broadening of both initial and final states was measured. Finally, a new surface state was observed on the Al(100) surface.

I. INTRODUCTION

Aluminum with the atomic configuration of $(Ne)3s^2 3p^1$ is the textbook example of a trivalent nearly-free-electron metal.[1] Ashcroft has shown that the Fermi surface[2] and optical properties[3] of aluminum can be explained by a nearly-free-electron band structure. This band structure can be produced with four plane-wave components and only two adjustable Fourier coefficients of the pseudopotential. The comparison of this nearly-free-electron band structure and the free-electron bands is shown in Fig. 1. The bottom of Fig. 2 shows the bulk Brillouin zone for a fcc solid. Figure 1 shows that the bands in aluminum are free-electron-like except near the Brillouin-zone boundary where there are degen-

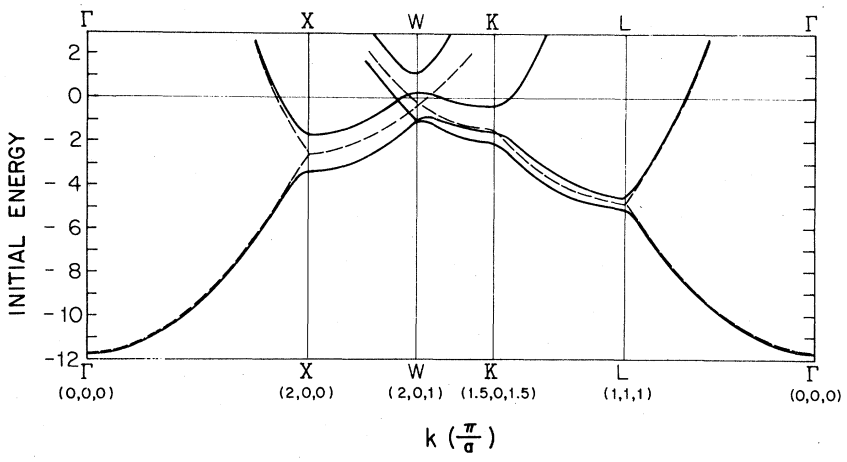

FIG. 1. Band structure of aluminum. The solid bands are calculated with the use of four plane waves and only the first two Fourier coefficients of the potential (Refs. 2 and 4). The Fourier coefficients were chosen to fit the Fermi surface. The dashed lines are the empty-lattice free-electron bands.

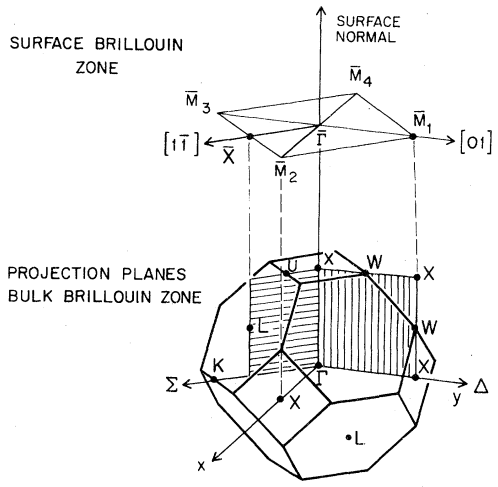

FIG. 2. Bulk and surface Brillouin zones for the (001) face of an fcc metal.

erate free-electron bands. These degenerate states are split by the weak periodic crystal potential.

The first two Fourier coefficients of the pseudopotential have been adjusted to fit the Fermi surface and optical properties.[2-4] This fit is obtained with V_{200} (ΓX in Fig. 2 lies along the positive x axis) in the range 0.76 to 0.84 eV and V_{111} between 0.25 and 0.25 eV.[2-4] This produces a gap of ~ 1.6-eV width at X and a smaller gap of ~ 0.5 eV at L. The gap at X moves up towards the Fermi energy as $\vec{k}$ goes from X to W along the Brillouin-zone boundary (see Fig. 1). How and where these bands cross the Fermi energy near W determines the shape of the Fermi surface in the third Brillouin zone of Al as well as the optical absorption.[1] More sophisticated band-structure calculations of aluminum reproduce the qualitative features shown in Fig. 1.[5,6(a)]

The concept of energy-band structure is fundamental to the theory of the electronic properties of crystals. Only recently, however, have there been direct experimental determinations of the band structure away from the Fermi surface, through the use of energy- and angle-resolved photoemission and synchrotron light sources. Nearly all of these studies have been concerned with the noble and transition metals or compound semiconductors. Here we have measured the band structure of a nearly-free-electron metal (aluminum) along the Γ to X and X to W directions in the bulk Brillouin zone. The results will be shown to agree qualitatively with the band structure presented in Fig. 1, but significant quantitative disagreement exists between our data and the best band-structure calculations.

The measurement of the dispersion of bulk bands using angle-resolved photoemission is not a direct process.[7,8] The energy and momentum of the emitted electron is measured in the vacuum so that the bulk is seen through the window of the two-dimensional surface Brillouin zone (SBZ) (Fig. 2). The parallel component of the momentum $k_{||}$ is conserved across the interface (moduli a surface reciprocal-lattice vector), so that for a given setting of the analyzer with respect to the crystal, the value of $k_{||}$ inside the bulk can be calculated from the experimental $\vec{k}$ value in the vacuum [$k_{||}=(2mE_{\rm KE}/\hbar^2)^{1/2}\sin\theta$, where $E_{\rm KE}$ is the photoelectron kinetic energy and θ is the detection angle measured from the surface normal]. The third component of the crystal momentum ($k_\perp$) inside the bulk cannot be determined unless the final-band structure is known along the rod in $\vec{k}$ space defined by $k_{||}=$const. This means that it is a complicated, iterative procedure to determine both the occupied and unoccupied band structure from these experiments. We have chosen to present this discussion in Sec. III so that in Sec. II the physics of the occupied band dispersion can be described without elaborate details of the photoemission process.

Section IV will compare our measured unoccupied bands with single-particle calculations. The lifetime (imaginary part of the self-energy) of both the initial- and final-band states in the photoemission process have been measured and will be discussed in Sec. V.

II. DISPERSION OF THE OCCUPIED BANDS

Only a short discussion of the photoemission process is given in this section so that it is clear which properties of the aluminum band structure can be measured directly and which depend upon a determination of the final band structure (Sec. III). We will show that the critical energies in the band structure at the high-symmetry points of the bulk Brillouin zone can be determined directly, but the detailed dispersion obtained from the photoemission data depends upon the actual shape of the final bands.

We view the photoexcitation process in the bulk as a "direct transition." This phrase denotes a transition between an occupied band characterized by E_i and $\vec{k}_i$ and an unoccupied band characterized by E_f and $\vec{K}_f$, such that both energy and momentum are conserved. This requires that

$$E_f=\hbar\omega-E_i\ , \tag{1a}$$

$$\vec{K}_f=\vec{k}_i+\vec{G}\ . \tag{1b}$$

The crystal furnishes the momentum in the photo-

excitation process by adding the bulk reciprocal-lattice vector $\vec{G}$. Equation (1b) is just the definition for folding an extended-zone state $\vec{K}_f$ back into the reduced-zone scheme. If we write the reduced-zone final crystal momentum as $\vec{k}_f=\vec{K}_f-\vec{G}$ then crystal momentum is conserved in the photoemission process $\vec{k}_f=\vec{k}_i$. This is the origin of the term vertical transitions. The transition is vertical in a reduced-zone scheme picture.

If the angle-resolving detector is aligned normal to an Al(100) crystal then the rod in the three-dimensional Brillouin zone defined by $k_{||}=0$ is along the Γ to X direction (see Fig. 2). We have plotted part of the reduced-zone structure in this direction for an empty lattice in Fig. 3. If we define the axis normal to the surface as the z axis, then $\vec{k}$ in the reduced-zone scheme is confined to the range $2\pi/a(0,0,-1)$–$2\pi/a(0,0,1)$ where $a=4.05$ Å at room temperature. The lowest energy band in Fig. 3 has the zero reciprocal-lattice vector associated with it. The second band has an extended-zone momentum $\vec{K}=\vec{k}-(2\pi/a)(0,0,2)$ and the third band has $\vec{K}=\vec{k}+(2\pi/a)(0,0,2)$. Both of these bands have an extended-zone momentum of the form $(0,0,k\pm4\pi/a)$ so that the excited electron propagates along the z axis normal to the surface. There are many more unoccupied bands then those shown in Fig. 2 (see Fig. 12 and Ref. 9), but they involve different reciprocal-lattice vectors, e.g., of the form $G_{111}=2-(\pi/a)(1,1,1)$ which generate final states $\vec{K}$ of the form $(2\pi/a,2\pi/a,k+2\pi/a)$. This wave does not come out in the normal direction. When the crystal potential is turned on the picture is not as simple because the bands folded back with different $\vec{G}$'s will mix and hybridize, if the symmetry allows for that. A detailed discussion of the final bands is given in Secs. III and IV.

The criteria for a transition are easy to determine using Fig. 3. The initial state must be occupied, i.e., below the dashed line which is the Fermi energy for a trivalent metal. The final band must have the same reduced momentum and be separated in energy from the initial state by the photon energy. We show in Fig. 3 the only allowed transition for $\hbar\omega=52$ eV. The initial state is ~10 eV below the Fermi energy and the final state is ~40 eV above the Fermi energy. The value of k is $\sim0.4(2\pi/a)$. It can be seen from Fig. 3 that if the photon energy is increased from 52 eV the value of k, where the transition occurs, will increase causing the initial-state energy to move closer to the Fermi energy. If the photon energy is decreased the value of k will decrease and the initial-state energy will move away from the Fermi energy. At a photon energy that matches the Γ points ($\hbar\omega=\hbar^2/2m[2(2\pi/a)]^2=37$ eV) the initial-state binding energy reaches its maximum so that, as the photon energy is decreased below 37 eV, the energy of the initial state involved in the transition moves back towards the Fermi energy. In general, such extrema in the observed binding energies correspond to transitions occurring at points of high symmetry in the Brillouin zone. The value of $\vec{k}$ is then known unambigously at these critical points.

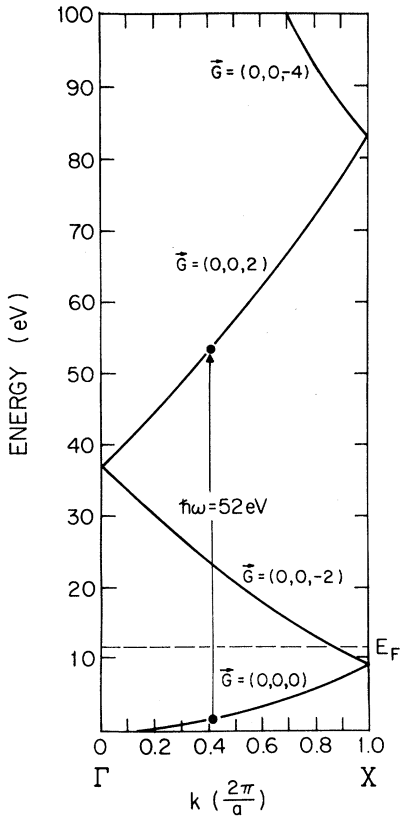

FIG. 3. Empty-lattice band structure along the Γ to X direction. Only those final bands are shown whose crystal momentum is parallel to the Γ to X direction.

Figure 4 shows a series of normal-emission photoelectron spectra as a function of photon energy. These curves are all shifted to align the Fermi edge, by defining an energy scale independent of photon energy,

$$E_i=E_{\mathrm{KE}}+\phi-\hbar\omega\ , \tag{2}$$

where E_{KE} is the measured kinetic energy and ϕ is the work function. The shaded peaks in Fig. 4 are the direct transitions that we described before. At $\hbar\omega=52$ eV the binding energy of the initial state involved in the transition is 9.4 eV compared to our 10-eV prediction from Fig. 3. As the photon energy is increased the direct-transition peak moves toward the Fermi energy. At much higher photon energies

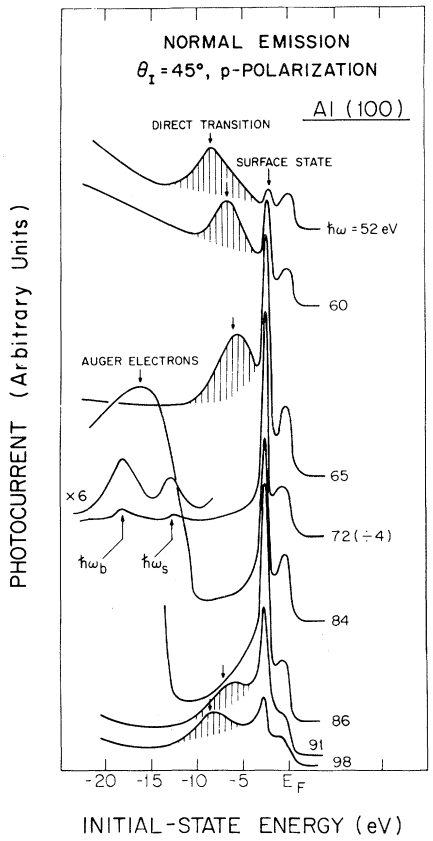

FIG. 4. Normal-emission photoelectron spectra plotted as a function of binding energy with respect to the Fermi energy.

it moves back away from the Fermi energy as Fig. 3 would predict. In the photon energy range between 70 and 80 eV no direct transitions could be resolved as a consequence of several problems. First, the transition is moving close to the intense surface-state (SS) peak at -2.75 eV which makes locating the energy position of the direct transition difficult. Second, for photon energies larger than 72 eV the $2p$ core level can be excited to above the Fermi energy, resulting in a large Auger signal in the valence-band region. The $\hbar\omega = 84$ and 86 eV spectra show this Auger peak moving away from the valence band. The third problem in this photon energy range is also related to core emission. The cross section for exciting the $2p$ core electron with second-order light from the monochromator is as large as the valence excitation with first order. Hence at $\hbar\omega = 70$ eV the second order at $\hbar\omega = 140$ eV excites the $2p$ core so that is appears in the spectrum approximately 2 eV below the Fermi edge. The $\hbar\omega = 72$ eV spectrum of Fig. 4 also has two small peaks approximately 13 and 18 eV below the Fermi level. These peaks are the surface- and bulk-plasmon losses off the intense surface-state peak. These losses follow the dispersion and intensity of the surface state and their energies are $\hbar\omega_b = 15.0 \pm 0.2$ eV and $\hbar\omega_s = 10.2 \pm 0.2$ eV, respectively.

Figure 5 shows the actual data for the initial-state energy of the observed direct transition versus the photon energy. The dashed line is the theoretical prediction from the free-electron bands shown in Fig. 3. There are several important conclusions that can be drawn from Fig. 5 without further data analysis.

(1) The free-electron band prediction is quite good, especially near the Fermi energy. The de Haas–van Alphen data of the second zone of aluminum show that the band is very nearly-free-electron-like and they provide us with the value of $\vec{k}$ at the Fermi energy (see Fig. 3).[4]

(2) The measured bandwidth of aluminum is ~ 1.2 eV less than the free-electron bandwidth. This can be determined directly from Fig. 5. The maximum depth of the initial state is seen around $\hbar\omega = 43$ eV.

(3) The presence of the gap at X can be seen near $\hbar\omega = 70$ eV. It is obscured in this data by excitation of the core level by second order from the monochromator, the presence of the surface state, and the Auger peaks seen in Fig. 4.

The second set of data which was accumulated, required an off-normal collection. $k_{||}$ was adjusted for each photon and binding energy to be at $k_{||} = (0, (2\pi/a))$. This is the $\bar{M}$ point in the surface

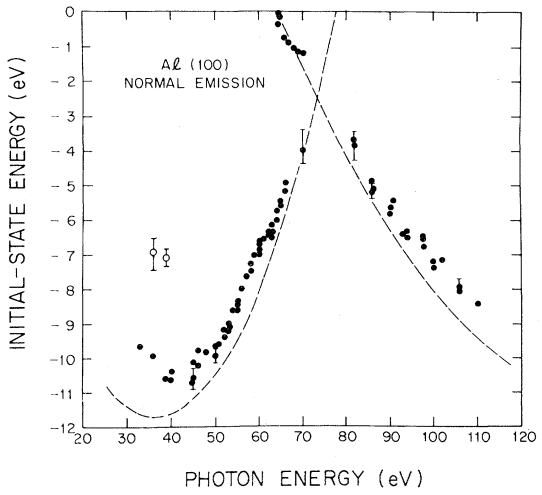

FIG. 5. Measured initial-state energy of the direct-transition peaks in normal emission from Al(100) as a function of photon energy. The dashed lines is the prediction from free-electron bands. Open circles are weak structures.

Brillouin zone and defines a rod in the three-dimensional zone as any $\vec{k}=(0,(2\pi/a),k_z)$ which is the line running from $X(0,(2\pi/a),0)$ to $W(0,(2\pi/a),\pi/a)$ in the reduced-zone scheme. An equivalent reduced-band picture to the one shown in Fig. 3 can be easily calculated for the X to W direction. Again we keep only those bands that have the correct direction in the extended-zone scheme. Figure 6 shows the measured initial-state energy versus photon energy for the range of $14<\hbar\omega<90$ eV. The dashed line is the free-electron empty-lattice prediction. The symmetry requirements associated with the various measurement geometries will be discussed in Sec. IV.

The following conclusions can be drawn from Fig. 6:

(1) The empty-lattice prediction (dashed line) is again pretty good, if we keep in mind that the degeneracy of the free-electron bands at the zone face will be lifted by the crystal potential (Fig. 1).

(2) The symmetry of the data around $\hbar\omega=18$ eV tells us where the W point is and consequently the initial-state energy of the doubly degenerate W_3 point: $W_3=0.90\pm0.05$ eV (see Fig. 1).

(3) The photon energy region between 30 and 40 eV shows the critical points in the band structure at X. From this data the bottom of the gap is at 2.83 ± 0.04 eV (X_4' point) and the top at 1.15 ± 0.04 eV (X_1 point). These critical points are determined without any assumptions for the final-state bands.

(4) The gap at X is not centered about the free-electron band. In the simple nearly-free-electron model the gap at X should have a magnitude of $2V_{200}$, symmetric about the free-electron band.[1]

Table I lists our experimentally determined energies at the high-symmetry points and compares them to various theoretically determined bands. Before we discuss this comparison in detail, the energy-band dispersion will be presented and compared to several calculated dispersions. Keep in mind that the detailed shape of the dispersion depends upon determination of the shape of the final-band structure (Sec. III). The energies at the symmetry points given in Table I are independent of our choice of final bands.

Figure 7 shows the occupied band dispersion along the Γ to X direction. The dashed line is the empty-lattice (free-electron) band and the dash-dotted lines are the bands deduced from fitting the Fermi-surface data.[15] This figure shows that the picture of aluminum being a nearly-free-electron metal is basically correct. The energy bands look parabolic except near the Brillouin-zone face, where a 1.68-eV gap exists. The energy bands deduced from the Fermi-surface topology[1,4] produce a gap of the correct magnitude, but 0.5 eV too far from the Fermi energy. The total bandwidth is experimentally 1.2 eV narrower than the free-electron or weak periodic potential bands.

The dispersion in the X to W direction is shown in Fig. 8. This direction is perpendicular to the Γ to X direction shown in Fig. 7 (see Fig. 2), so the data start at the gap at X seen in Fig. 7 and go to W. The dotted line is the free-electron band and the dashed curves are the bands deduced from fitting the Fermi surface to a simple four-plane wave, two-Fourier-coefficient model.[1,4,15] In this model the two energies at X will be

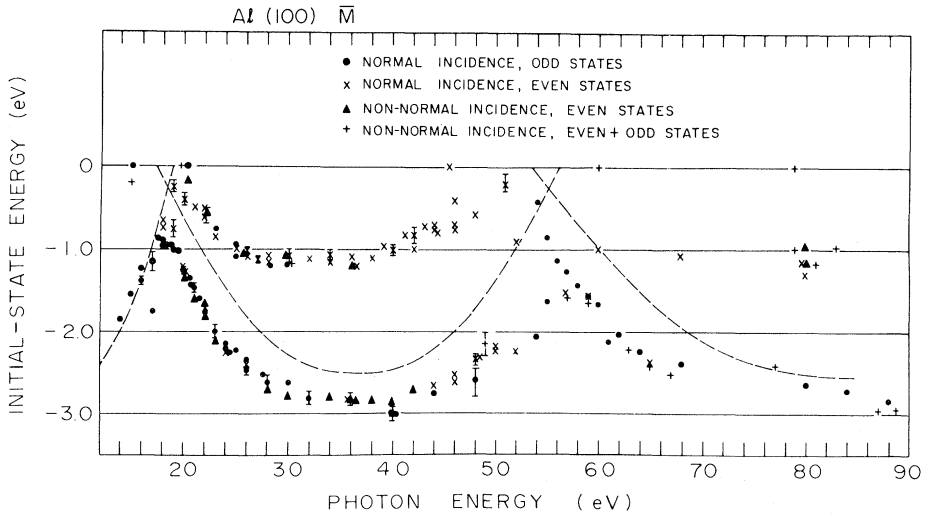

FIG. 6. Initial-state energy of the bulk transitions along the XWX rod in the bulk Brillouin zone (Fig. 2). The dashed line is the prediction from the free-electron bands. The different symbols are different measurement geometries.

TABLE I. Critical points in the aluminum band structure.

Symmetry points	Experimental value	Fermi-surface fitting (Ref. 4)	Pseudo-potential (Refs. 10 and 11)	Model potential[a]	Self-consistent LGGO (Ref. 5)	Augmented plane wave (Ref. 6)
Γ_1 (bandwidth)	-10.6 ± 0.2 eV	-11.8 eV	-11.50 eV	-11.7 eV	-11.1 eV	-11.05 eV
X_1	-1.15 ± 0.04	-1.66	-1.7	-1.43	-1.64	-1.77
X_4'	-2.83 ± 0.04	-3.31	-3.2	-3.07	-2.96	-2.76
Gap at X	1.68 ± 0.08	1.65	1.5	1.64	1.32	0.99
W_3	-0.90 ± 0.05	-0.99	-0.97	-0.84	-0.90	-0.67
L_2'	-4.55[b]	-5.07	-4.9	-4.76	-4.62	-4.53
L_1		-4.62	-4.5	-4.45	-4.41	-4.33
Gap at L		0.45	0.4	0.31	0.21	0.20
K_3				-1.93	-1.40	-1.72
K_1				-1.34	-1.93	-1.33
K_1	-0.75 ± 0.2			-0.18	-0.4	-0.59

[a]Nelson and Bunyan (Ref. 12) used the Heine and Abarenkov (Ref. 13) model potential theory and Shaw's (Ref. 14) optimized model potential to calculate the band structure of Al.
[b]Binding energy of surface state in gap at L.

$$E_1=\frac{\hbar^2}{2m}\left[\frac{2\pi}{a}\right]^2-V_{200}\,, \tag{3a}$$

(X_4') is p-like,

$$E_2=\frac{\hbar^2}{2m}\left[\frac{2\pi}{a}\right]^2+V_{200}-\frac{4V_{111}^2}{\frac{\hbar^2}{2m}\left[\frac{2\pi}{a}\right]^2}\,, \tag{3b}$$

(X_1) is s/d-like.

The solutions at W will be

$$E_1=\frac{\hbar^2}{2m}\left[\frac{2\pi}{a}\right]^2\frac{5}{4}-V_{200}\,, \tag{4a}$$

(W_3) is p/d-like,

$$E_2=\frac{\hbar^2}{2m}\left[\frac{2\pi}{a}\right]^2\frac{5}{4}+V_{200}-2V_{111}\,, \tag{4b}$$

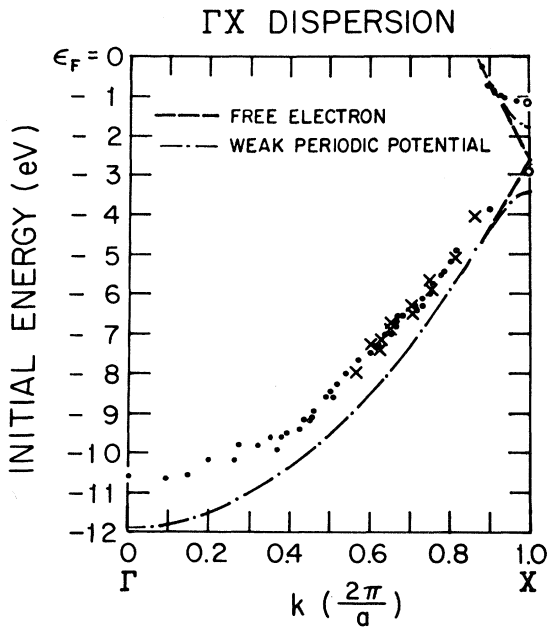

FIG. 7. Initial-state dispersion along the Γ to X bulk direction. The dashed curve is the free-electron band and the dash-dotted curve is the band structure obtained by fitting the Fermi surface (Refs. 4 and 15). The data points indicated by the circles are taken from Fig. 6.

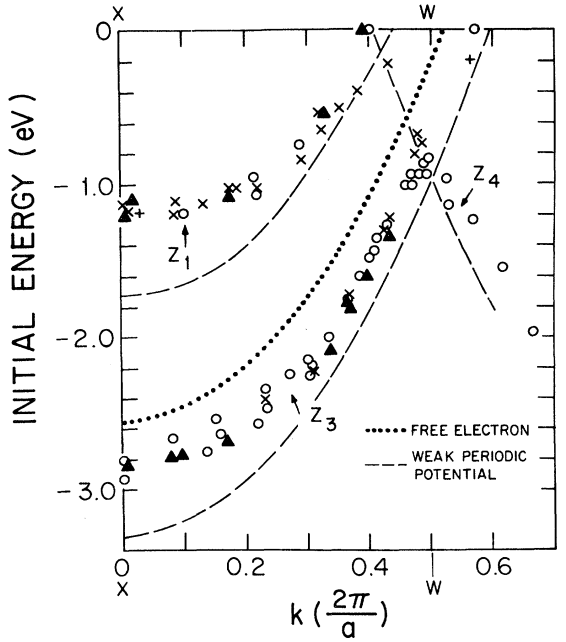

FIG. 8. Initial-state dispersion along the X to W bulk direction. The dotted curve is the free-electron band. The dashed curves are the band structure obtained by fitting the Fermi surface (Ref. 4). The symbols are explained in Fig. 6.

(W_2') is p/d-like, and

$$E_3=\frac{\hbar^2}{2m}\left[\frac{2\pi}{a}\right]^2\frac{5}{4}+V_{200}+2V_{111}\,, \tag{4c}$$

(W_1) is s/d-like. The values of V_{200} and V_{111} used were 0.84 and 0.24 eV, respectively.[15]

Figure 8 shows that the degeneracy in the free-electron bands at the zone face is removed by the periodic potential. The main problem, however, is clear; the measured bands are not centered about the free-electron band as Eq. (3) would predict [the contribution from V_{111} in Eq. (3b) is only 0.025 eV, compared to 0.84 eV from V_{200}]. The center of the gap is shifted up by $\sim$0.5 eV with respect to the free-electron band. A second less obvious discrepancy is observable if the values in Table I are compared to Eqs. (3) and (4). The band connecting the bottom of the gap at X with W should be free electron in shape, shifted down by V_{200} with respect to the free-electron band. At X the difference between the free-electron band and the measured bottom of the gap is 0.24$\pm$0.04 eV. At W this difference is 0.60$\pm$0.05 eV. This means that the experimental band is not free-electron-like, in fact, it can be fitted quite well by an effective-mass band with $m^*=1.18m$.

The discrepancies between the experimental bands and the calculated bands shown in Figs. 7 and 8 may well be a consequence of the simple theoretical model used. The fact that these theoretical bands fit the Fermi surface and low-energy optical data,[1,3,4] does not assure that they are correct far away from the Fermi energy. Therefore, we present in Figs. 9 and 10 a comparison of our data with the self-consistent linear combination of Gaussian orbitals (LCGO) calculation by Singhal and Callaway.[5(a)]

Figure 9 and Table I show that the bandwidth in the self-consistent band calculation is closer to the experimental value than the free-electron (or nearly-free-electron) bandwidth. However, there is still a measurable difference between theory and experiment in the position and shape of the bottom of the band. Furthermore, the gap at X is not positioned correctly, the X_4' point is correct, but the X_1 point is calculated to be too far from the Fermi energy, resulting in a gap which is too small by $\sim$20%. This is seen clearer in the X to W direction shown in Fig. 10. The shape of the calculated Z_3 band from X to W is correct. Singhal and Callaway's calculated Z_3 band has an effective mass of $\sim$1.15 where our experimental band has an effective mass of 1.18$\pm$0.05.

Let us summarize the comparison of the data with the self-consistent LCGO calculation:

(1) The experimental bandwidth is still smaller than the calculated value, 10.6 eV compared to 11. 1

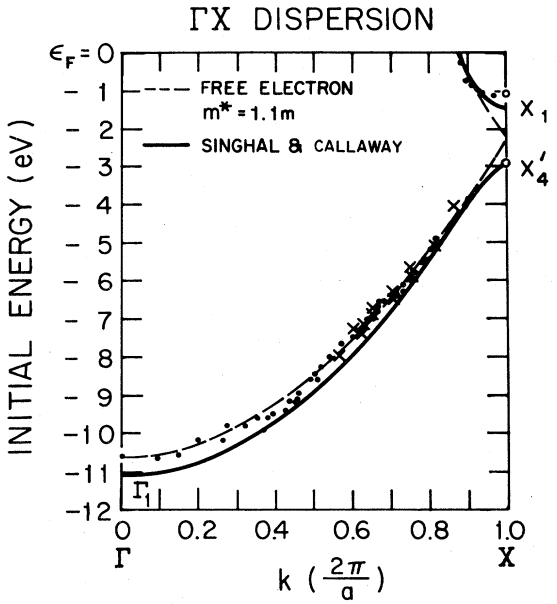

FIG. 9. Comparison of the experimental dispersion from Γ to X to theoretical calculations by Singhal and Callaway [Ref. 5(a)]. The dashed line is an effective-mass band with $m^*=1.1m$ (data for $\hbar\omega<70$ eV, $\hbar\omega>70$ eV).

eV. This can be rephrased in terms of an effective mass. The band calculations predict an effective mass at the bottom of the s band of $m^*=1.04m$, while our experimental band is best fitted by an effective mass of 1.10$\pm$0.02.[16]

(2) The gap at the X point is theoretically too

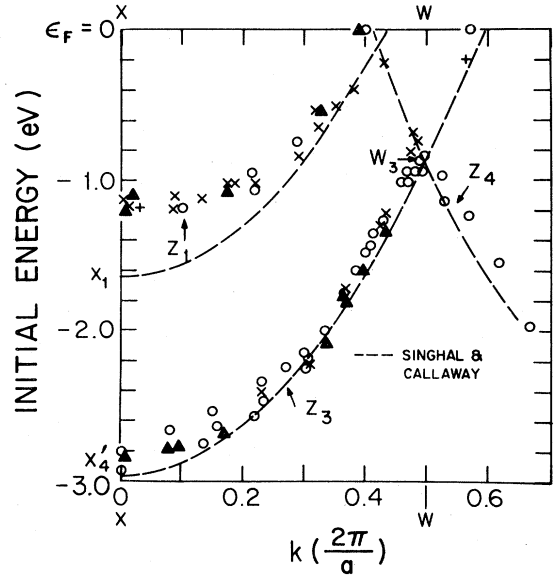

FIG. 10. Comparison of the experimental dispersion from X to W with theoretical calculations by Singhal and Callaway [Ref. 5(a)].

small, 1.32 eV compared to 1.68 eV, experimentally. Almost all of the error is at the X_1 point. The calculated value is 0.5 eV too far from the Fermi energy.

(3) The shape and position of the Z_3 band in the calculation is in very good agreement with the data. This band has an effective mass of $m^*=1.18m$.

We will now attempt to address the physical origin of the two points of discrepancy between theory and experiment; the bandwidth and the X_1 point. There is a consistent and reasonable explanation for the reduction in the bandwidth. Any theoretical calculation using a local density approximation for exchange and correlation ignores the nonlocal portion of the self-energy.[17,18] The calculations are correct at E_f but deviate when the energy differs from E_f. Hedin *et al.* have calculated the nonlocal self-energy for jellium, showing that it reduces the free-electron bandwidth by about 5%, nearly independent of electron density.[19] This means that the effective mass of the correlated band is $\sim 1.05m$. The calculation of Singhal and Callaway[5(a)] or Szmulowicz and Segall[6(a)] yield an effective mass of $\sim 1.04m$ for the bottom s band, resulting from the periodic potential. The two effects should be additive, yielding an effective mass for the bottom of the s band of $\sim 1.09m$, which agrees with the experimental result of $m^*=1.10\pm 0.02m$.

This effect should be quite general. The measured width of the s band should be $\sim 5\%$ less than the value calculated by the best self-consistent local density calculation. The measured bottom of the s band in Cu is at 8.6 eV,[20] while the theoretical prediction of Burdick[21] is 8.9 eV, a 3% reduction. The calculations of Janak, Williams, and Moruzzi[22] give a bandwidth of 10 eV for Cu, which means that the experiment differs by 14%.

An explanation of the differences in the theoretical and experimental points at X is not immediately obvious. The first observation which can be deduced from Table I is that the experimental magnitude of the gap agrees much better with the early, less sophisticated theoretical calculations than with the more recent self-consistent schemes, which shift the gap up towards E_f, but reduce its magnitude. Both Singhal and Callaway[5] and Szmulowicz and Segall[6(a)] give acceptable answers for the p state X_4': 2.96 and 2.76 eV compared to 2.83 eV experimentally. The s/d-like X_1 point, however, is calculated to be at 1.64 and 1.77 eV, respectively, compared to 1.15 eV, experimentally. It is interesting to note that neither of these two calculations gives a complete explanation of the low-energy optical data of aluminum.[23] Singhal and Callaway's band structure reproduces the principle absorption peak at $\hbar\omega=1.6$ eV very well, but might be significantly off for the second maximum at $\hbar\omega=0.5$ eV.[5(b)] Szmulowicz and Segall,[6(b)] on the other hand, have to use a parametrized band structure, which increases the gap at X to 1.56 eV ($X_1=-1.6$ eV, $X_4'=-3.16$ eV) to obtain agreement with the measured optical conductivity. Furthermore, the two calculations assign different regions in $\vec{k}$ space as being responsible for the parallel-band absorption peak at $\hbar\omega=1.6$ eV (near W point[5(b)] or the vicinity of Σ axis.[6(b)]).

There is also a potential experimental problem associated with measuring the X_1 point. The energy bands near X_1 disperse towards the Fermi surface in all directions as one moves away from X. Any smearing in $\vec{k}$ resolution, either experimentally or physically, would result in a measurement which is an average over a region of $\vec{k}$ space around X. This could give an experimental binding energy at X_1 smaller than the actual energy and needs further consideration. There are two mechanisms for $\vec{k}$ smearing:

(1) The analyzer has a $\pm 2.5°$ collection angle, which means we sum over a small range of $k_{||}$ (the uncertainty due to the energy resolution is an order of magnitude smaller in the present energy range).

(2) The final state in the photoexcitation process has a short lifetime, resulting in an uncertainty in energy, or a short mean free path, resulting in an uncertainty in $\vec{k}$.

The experimental contributions due to the analyzer can be calculated. At $\hbar\omega=30$ eV the analyzer is set at 37.8° so that a peak 1.2 eV below the Fermi energy corresponds to $k_{||}=\bar{M}$. The 2.5° half angle of the analyzer produces a $\Delta k_{||}=0.08$ Å^{-1} which is $\sim 5\%$ of the zone-edge value of $k_{||}$. If we know the initial and final band structure then the average of the direct-transition energy over this area in $k_{||}$ space could be calculated and compared to the energy at X_1 or X_4'. The initial-state energy near X_1 can be approximated by

$$E_2=E_0(1+\vec{k}^{\,2})+2E_0\left[k_y^2+\frac{V_{200}^2}{4E_0^2}\right]^{1/2}, \qquad (5)$$

with $E_0=(\hbar^2/2m^*)(2\pi/a)^2$ and all k's are measured in units of $2\pi/a$ with the origin at X. k_y is measured from X towards Γ. It is in this directions that the bands disperse most rapidly away from X_1 towards E_f. In either the $X\rightarrow W$ or $X\rightarrow U$ direction (see Fig. 2) the bands are nearly-free-electron-like and show only a small upwards dispersion near X (see Figs. 1 and 8).

If we assume that the final bands near X are free electronlike, then the error in measuring the X_1 point with a given $\Delta k_{||}$ resolution can be calculated. We use a constant matrix element so the measured energy at X_1 is the direct-transition energy weighed

by the joint density of states at a specific k integrated over the smearing in $k_{||}$. This integral gives for a $\Delta k_{||}=0.08$ Å^{-1} a predicted shift in X_1 which is smaller than our experimental uncertainty. The data at $\hbar\omega=80$ eV also substantiate this conclusion. At this high photon energy the $\pm 2.5°$ angular resolution translates into $\Delta k_{||}=0.18$ Å^{-1}. There is no major distortion at X_1 due to the finite angular collection, because the rapidly dispersing bands have a low density of states.

We will show subsequently that the final bands near X are not free-electron-like. In fact, there is a $\sim$6-eV gap in these bands which means that near X the final bands will be nearly flat. Flat final bands will reduce any potential error in the measurement of the critical points due to finite angular resolution.

The k smearing caused by the finite lifetime of the final states has only a small effect on the apparent binding energy of the X_1 point. In a subsequent section we will calculate the uncertainty in $\Delta k_\perp$ from our data. $\Delta k_\perp$ ranges from 0.08 Å^{-1} to 0.14 Å^{-1} for energies 30–90 eV above E_F (see Sec. IV). Since this uncertainty is constrained only to $k_\perp$, which is along the X-W axis in our measurement, there will be an insignificant shift in the measured energy of the X_1 point compared to the real X_1 point energy. If this $k_\perp$ smearing was important we would see a systematic difference in the binding energies near $\hbar\omega=30$ eV and $\hbar\omega=80$ eV. The measured X_1 (X_4') binding energy at 80 eV would be smaller (larger) than at 30 eV.

Thus from the experimental point of view the critical-point energies X_1 and X_4' are exact. The measured gap at X is, therefore, larger in magnitude and closer to the Fermi energy than calculated. It remains to be seen whether this discrepancy is due to the uncertainties in the effective potential (including exchange and correlation[6(b),14]) used in the calculations, or the difference between an excitation spectrum and a ground-state band structure.

III. PHOTOEMISSION ASPECTS

A. Experimental

All of our data were taken with a constant-transmission spectrometer which has an angular resolution of $\pm 2.5°$.[24] The energy resolution could be varied by adjusting the pass energy of the hemispherical analyzer. The light from the electron storage ring Tantalus at the University of Wisconsin was dispersed by a toroidal grating monochromator.[25] The bandpass of the monochromator was varied in order to maintain adequate resolution and photon flux for good counting statistics. The incident photon flux was monitored with a tungsten mesh photodiode.[26] The polarization was estimated to be $\sim$95%.[25]

The aluminum crystals were oriented to within 0.5° of the (001) plane by Laue diffraction and subsequent spark planing and polishing. The polishing technique is known to produce extremely smooth surfaces, the surface disorder being below the detection limits of typical low-energy electron diffraction (LEED) instruments.[27] The principle surface contaminant was oxygen. This was removed by argon-ion bombardment, followed by annealing to 400°C for typically 15 min. The data shown here were taken with less than 1% of a monolayer of oxygen on the surface.[28]

The crystal was mounted on a two axis of rotation manipulator, and the orientation determined both by grazing incidence electron diffraction and the position of the surface state in the second and third surface Brillouin zones. When measurements were made off normal at a fixed $k_{||}$, an iterative procedure was used. The angle of collection for a given photon energy and initial-state energy was calculated, an energy distribution collected at this setting and then a new angle calculated based on the binding energy of the observed peak. Usually two or three iterations were necessary for $\hbar\omega<30$ eV.

The experimental chamber and monochromator were pumped with ion pumps and Ti sublimation pumps. The monochromator pressure was in the low-10^{-11} Torr range and the sample chamber in the low-10^{-10} Torr range. The sample was normally sputtered and reannealed every 5 h.

B. Determination of the final band structure

The photoemission spectra as a function of $\hbar\omega$ measure the separation in energy between the initial and final states and the energy below the Fermi energy of the initial state. Since the transition is direct, both the initial and final states have the same reduced value of $\vec{k}$. The angle-resolved detector picks out a specific value of $\vec{k}_{||}$, leaving only $k_\perp$ to be determined. If we know the dispersion of the initial-state band, we can use the data to calculate the final-state dispersion or vice versa.

By far the most common practice is to assume that the final bands are free electronlike.[29] Knapp *et al.*[30] made significant improvement upon this procedure by measuring portions of the final bands and then fitting a calculated band structure to the data. They measured critical points and the photon energy where the initial band crossed the Fermi energy and used the measured Fermi-surface topology to find $\vec{k}$. Our approach with Al is to attempt to determine the final and initial bands in an iterative

procedure without relying on any theoretical calculation. This is possible due to the simplicity of the occupied bands in Al.

1. *Normal emission:* Γ *to* X

The surface state in normal emission is 2.75 eV below the Fermi energy which is within 0.1 eV of the band edge at X_4' (see Fig. 4). Therefore, the surface state is composed primarily of states of the same character and $k_{||}$ value as the X_4' bulk states and it penetrates deep into the bulk.[8] Louie *et al.*[31] showed that the cross section for photoexcitation of a surface state like this will peak when the photon energy is correct to excite it into a final bulk band with a value of $\vec{k}$ corresponding to the band extremum. This allows us to measure the final-band critical points at X. Figure 11 shows the measured intensity of the surface-state peak in normal emission (first zone) and at $k_{||}=2.19$ Å^{-1}, which is $\bar{\Gamma}$ of the second surface Brillouin zone. There are two intense peaks at $\hbar\omega=71$ and 74 eV in normal emission and one major peak at $\hbar\omega=48$ eV in the second-zone emission. The empty-lattice free-electron bands would have predicted energies of 73 and 46 eV, respectively, for the two zones.

The origin of the weak structures in the cross sections shown in Fig. 11 is not clear. They cannot be explained by the same coupling mechanism to a bulklike final state (none of the final states have the correct location in k space) nor is an atomic origin due to the $2p$ threshold at $\hbar\omega\sim72$ eV very likely, since the structures depend on the position in the surface Brillouin zone. However, it is possible that the dip in the $\bar{\Gamma}(2)$ emission at $\hbar\omega\sim73$ eV is caused by an interference of the emission from $\bar{\Gamma}(1)$ and $\bar{\Gamma}(2)$, whereby a surface reciprocal-lattice vector is involved. This could lead to a Fano-type line shape for the surface-state intensity at $\bar{\Gamma}(2)$.

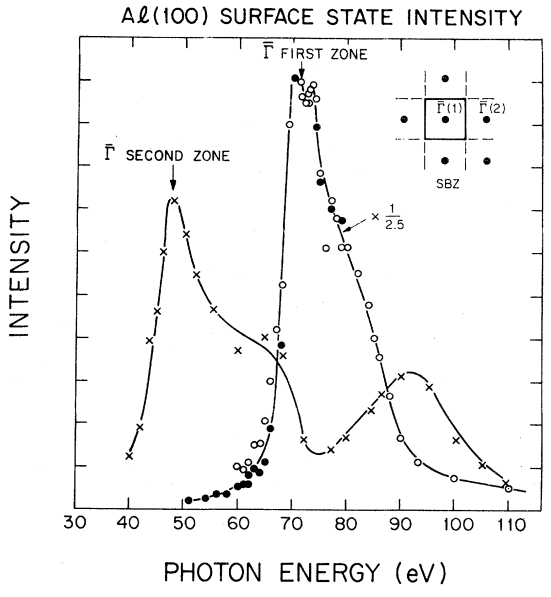

FIG. 11. Photoionization cross sections for the surface state at $\bar{\Gamma}$ in the surface Brillouin zone (SBZ). One curve is for the first Brillouin zone $\bar{\Gamma}(1)$ ($k_{||}=0$) and the other for the second Brillouin zone $\bar{\Gamma}(2)$, as shown in the inset.

The surface-state cross section for the first zone shown in Fig. 11 gives two points of the final band structure at X. These points are at 68 and 71 eV above the Fermi energy. A third point can be obtained from the Fermi-energy crossing at $\hbar\omega=64$ eV seen in Fig. 5. The fitting procedure of Anderson and Lane[4] to the second-zone de Haas–van Alphen data gives a value of $k_f=0.875(2\pi/a)$. Another restriction to the final bands is imposed by the measured bottom of the occupied band in the photon energy range $\hbar\omega=37-45$ eV (Fig. 5).

The experimentally determined final bands in the Γ to X direction are shown in Fig. 12(a). The measurements discussed above, where $k_\perp$ was known, are shown by open circles. All of the other data points are plotted assuming a specific dispersion for the initial band. The closed circles represent the data of Fig. 5 plotted as a final band dispersion, using Singhal and Callaway's calculated dispersion for the occupied bands.[5(a)] The data points produced in this fashion agree with the E and k positions determined from the Fermi-energy crossing and the X point, but do not give an acceptable dispersion near Γ. The crosses in Fig. 12(a) are the final band dispersion obtained from the data of Fig. 5 assuming a free-electron initial state with an effective mass of $m^*=1.1m$.

Figure 12 shows that the final bands are nearly-free-electron-like except near Γ at an energy around 30 eV. The final bands determined from Singhal and Callaway's initial band do not produce final bands that reach Γ, because the occupied bandwidth is larger than the measured width. We experimented with initials bands of different effective masses, maintaining 3 e/at. An effective mass of $1.10m$ gives the best final-band structure. For $m^*<1.1$ the final bands do not reach Γ and for $m^*>1.1m$ there are data points lying below the bottom of the occupied band. Note that the assumption of the shape of the initial band has little or no effect for $k>0.3(2\pi/a)$. The dashed line in Fig. 12 shows the final band used to calculate the initial-state dispersion shown in Fig. 7. The data points in Figs. 7 and 12 are not completely independent of each other when using such an iterative procedure, which only works for the case of a simple initial-state band structure.

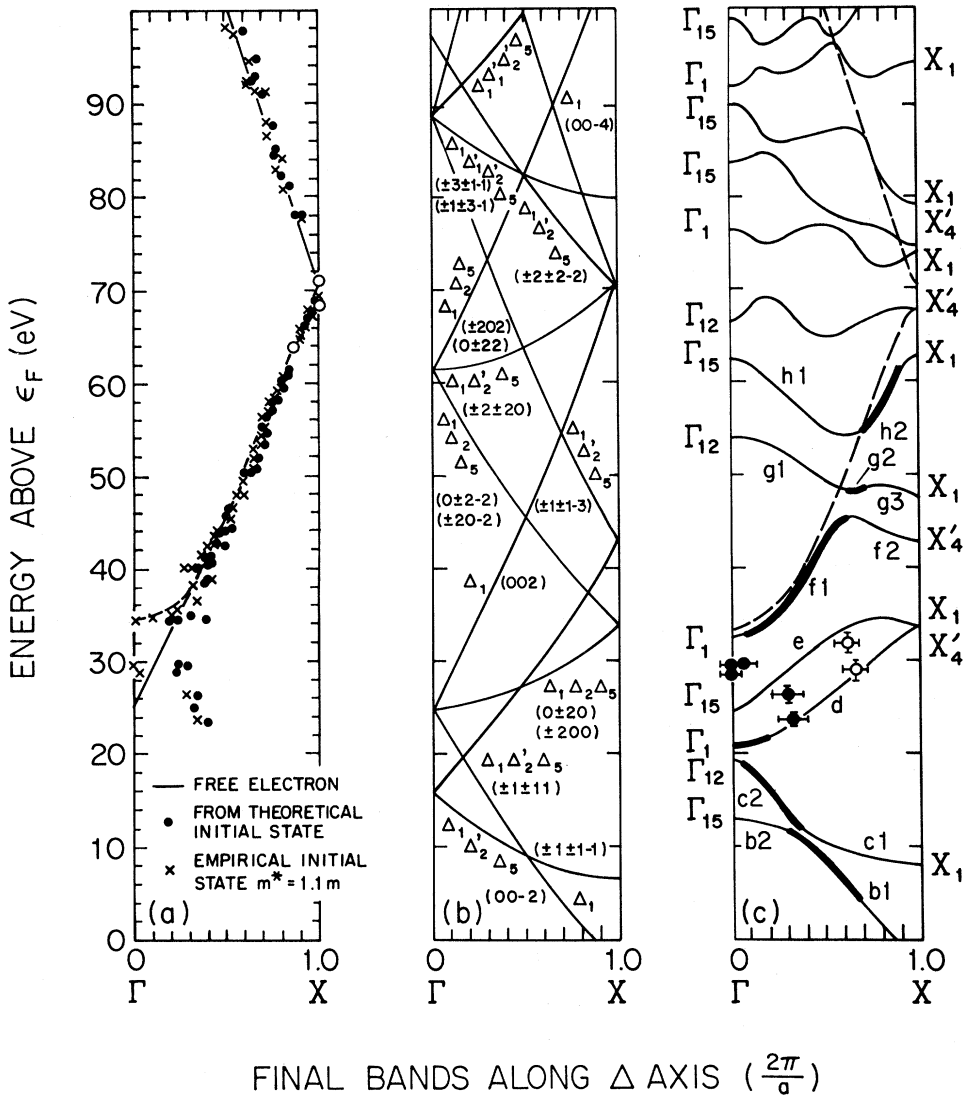

FIG. 12. (a) Experimental, (b) free-electron, and (c) calculated final bands (Refs. 32 and 9) along Γ-X. Open circles are uniquely determined points and dashed lines are best fit to data.

2. *Non-normal emission: X to W*

The dispersion of the final bands in the X to W direction was determined in a similar fashion to the Γ to X bands discussed above, except that there is more information about the initial-state dispersion in this direction. The Fermi-surface crossings along X to W are at 0.4 ($2\pi/a$) for the Z_4 and at 0.43 ($2\pi/a$) for the Z_1 band, as determined by Anderson and Lane[4] (see Fig. 8). Figure 13 show the photoemission intensity at the Fermi energy as the photon energy is changed with $k_{||}$ fixed at $\bar{M}$. A peak in the emission intensity is expected whenever a direct transition disperses through the Fermi level or when there is a high local density of final states. There are three different geometries of collection shown, which have bearing on the symmetry of the initial states and will be discussed in Sec. IV. These Fermi-surface crossings are shown in Fig. 14 as the circled data points.

A Z_3 initial-state band is constructed from the measured critical-point energies and the surface-state dispersion. In Fig. 15 we have plotted the dispersion of the surface state in both the $\bar{\Gamma}\bar{X}$ and $\bar{\Gamma}\bar{M}$ directions of the surface Brillouin zone, as measured by Gartland and Slagsvold[33] and Hansson and Flodstrom.[24] The dashed line is a free-electron parabola with an effective mass of $m^* = 1.18m$. Some

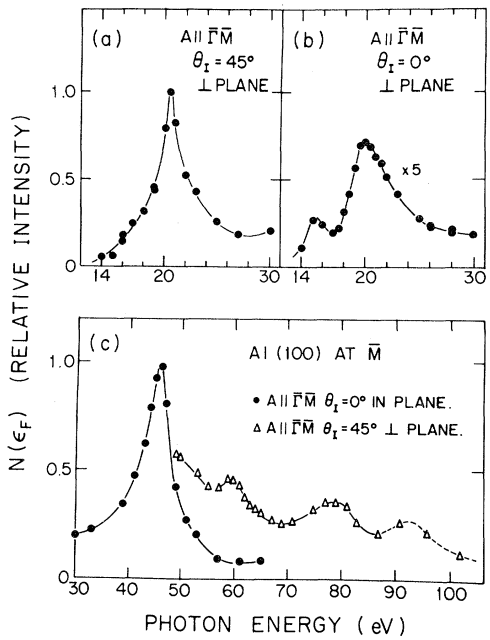

FIG. 13. (a) Intensity vs photon energy for a fixed initial state at 0.15 eV below the Fermi energy. (b) Different geometries and photon energy ranges are shown. (c) $k_{||}$ is fixed at $\bar{M}$.

of the data points at larger $k_{||}$ deviate from this line due to the large angular acceptance used in the experiment.[33] A careful inspection of Figs. 1 and 2 reveals that the dispersion of the gap in the projected band structure in the $\bar{\Gamma}$ to $\bar{M}$ direction of the surface Brillouin zone is determined by the dispersion of the Z_3 and Z_1 bulk bands in the X to W direction.[35,36] At $\bar{\Gamma}$ the surface state is only ~ 0.1 eV above the bottom of the gap. We assume that the Z_3 band follows the surface-state dispersion, i.e., we assume an effective-mass band with $m^* = 1.18m$. The solid curve in Fig. 15 shows this constructed band. It crosses X, W, and the Fermi energy at the appropriate E and k, respectively. The data points in Fig. 14(a) were obtained using the initial-state band and only the data in Fig. 6 for the lower (Z_3) band. The dashed lines in Fig. 14(a) are the final bands used to calculate the initial-state dispersion for both the Z_1 and Z_3 band. The final bands are nearly-free-electron-like except for a $\sim$6-eV band gap at X near 35 eV above E_F and for energies above 50 eV. The discrepancy above 50 eV as well as the justification for using the same final bands for Z_1 and Z_3 initial states will be discussed in Sec. IV.

C. Surface states along $\bar{\Gamma}\bar{X}$

The gap in the surface-projected band structure at $\bar{\Gamma}$, which is caused by the gap at X in the bulk-band structure, disperses up towards the Fermi energy as $k_{||}$ increases. This gap disappears for $k_{||} \gtrsim 0.5(2\pi/a)$. In the $\bar{\Gamma}\bar{X}$ direction a small gap exists for $k_{||} > 0.5(2\pi/a)$ which moves away from E_F as $k_{||}$ increases.[35,36] At $\bar{X}$ this gap will correspond to the gap at the L point in the bulk Brillouin zone (see Fig. 2). The inset at the top of Fig. 16 shows the calculated band structure along the rod defined by $k_{||} = \bar{X}$.[35] Two theoretical calculations have predicted a surface state in this gap.[35,36]

We have used the coupling of a surface state to bulk final bands at the critical points[31] to identify the surface state in this gap. Some spectra at $k_{||} = \bar{X}$ are shown in Fig. 16. The angle of the analyzer was adjusted to keep the peak at -4.55 eV at the appropriate $k_{||}$. There are two dispersing bulk peaks seen in the spectra and a peak with fixed binding energy at -4.55 eV, marked by the vertical line. This surface state can only be seen when the photon energy is near the resonant condition with the final band at L. The free-electron model predicts the resonance at $\hbar\omega = 19$ eV while Fig. 16 shows that the maximum intensity is at $\hbar\omega = 20$ eV. The calculations of Spanjaard *et al.*[35] find the surface state near the bottom of the gap at L, i.e., near the L_2' point. The measured binding energy of the surface state at $\bar{X}$ lies within the gap calculated by Singhal and Callaway[5(a)] (-4.41 to -4.62 eV) but is slightly outside of the gap calculated by Szmulowicz and Segall[6] (-4.33 to -4.53 eV). The free-electron value at L is -4.85 eV for $m^* = m$ and -4.41 eV for $m^* = 1.1m$.

The rod defined by $k_{||} = 1.5\bar{\Gamma}\bar{X}$ runs through the K point in the bulk Brillouin zone (Fig. 2). At this value of $k_{||}$ the surface state has a binding energy of ~ 1.9 eV (see Fig. 15). The emission from the surface state has a maximum at $\hbar\omega \sim 40$ eV, which locates the final band at K. The free-electron final bands would have predicted a resonance at 37.5-eV photon energy.

IV. FINAL BAND DISPERSION AND PHOTOEXCITATION INTENSITIES

The experimentally determined unoccupied bands are plotted in Figs. 12(a) ($\Gamma\Delta X$) and 14(a) (XZW). They are nearly-free-electron-like except near the zone center at Γ or the zone edge at X. In contrast the calculated band structure for this energy range in Al is very complicated and not free-electron-like.[9,37,38] For example, if we start with the free-electron bands in the $\Gamma\Delta X$ direction [Fig. 12(b)] and turn on a crystal potential, most of the degenerate free-electron bands are split. This results in at least 40 different bands along Γ to X in the first hundred electron volts above the vacuum level.[9] Strong devi-

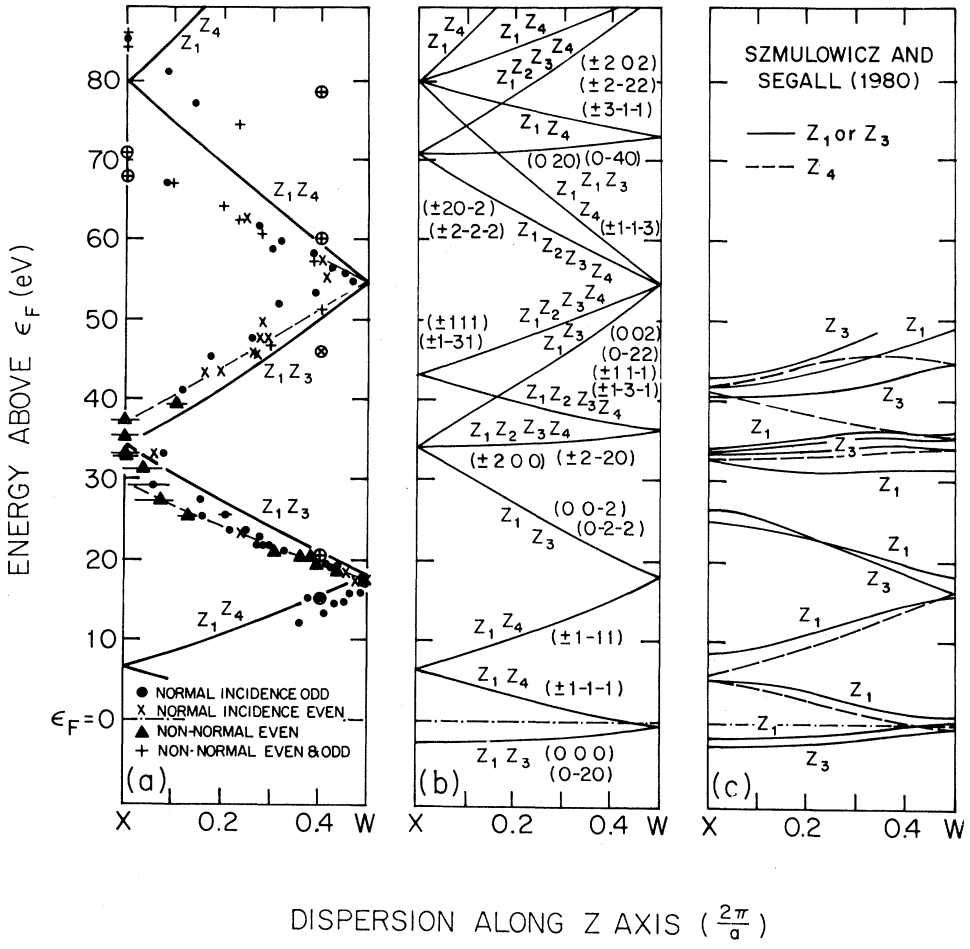

FIG. 14. (a) Experimental, (b) free-electron, and (c) calculated final bands [Ref. 6(a)] along XZW [$k=(0,1,k_z), 0\le k_z\le\frac{1}{2}$]. Circled points are determined from Fermi-surface crossings. The dashed line is the best fit to the data.

ations from the free-electron behavior are expected for Al in this energy region due to the presence of the unoccupied $3d$ and $4f$ levels. These unoccupied states can be seen in x-ray absorption spectra[6,37] or in angular momentum decomposition of the calculated energy bands.[38] The most intense d- and f-like features in the l-projected density of states are observed at 20–25 eV and ~35 eV above E_F, respectively.[38] As a result the calculated band structure of the final states is very complex [see Figs. 12(c) and 14(c)] and does not resemble our experimentally determined bands. We will show that this is an artifact of the photoemission experiment and is caused by symmetry restrictions, the surface matching conditions for wave functions at the solid-vacuum interface, and the strong inelastic processes in the photoemission final state.

The objective of this section is twofold. First, we will present a rationale for the apparent discrepancy between our measured final band dispersion and the calculated band structure and then we will address the issue of apparent violations of symmetry rules in the data for the X to W direction.

The easiest way to proceed is to start with the free-electron (empty-lattice) final bands and then discuss the effects of the crystal potential and the strong inelastic damping in the photoemission final state. The following discussion is divided into two sections, the first for the normal emission (Γ to X) and the second for the off-normal (X to W) data.

A. Normal emission, Γ to X

In normal emission the final state must be totally symmetric under all point-group operations of the surface. Accordingly, only Δ_1 final bands contribute to normal emission.[39,40] The empty-lattice bands with this symmetry are shown in Fig. 12(b) with the corresponding reciprocal-lattice vectors indicated. Figure 12(c) shows the calculated bands with Δ_1

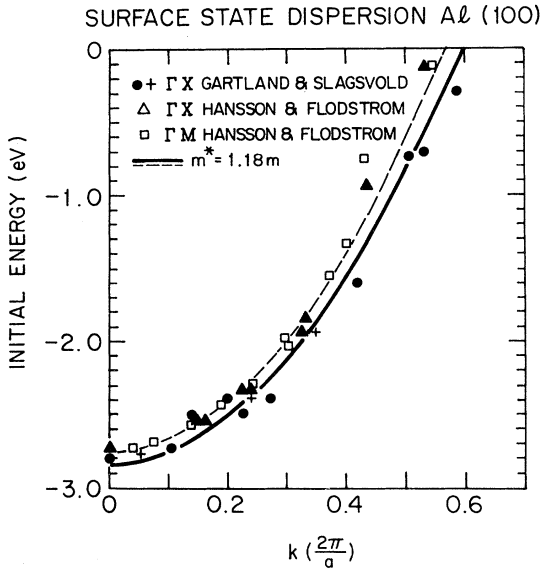

FIG. 15. Dispersion of surface state on Al(100) (Refs. 33 and 34). The dashed curve is a fit to the data by a free-electron band with $m^* = 1.18m$. The solid curve is a proposed Z_3 band with correct X, W, and Fermi-surface crossings.

symmetry. The energy range 0—60 eV is taken from Ref. 32 while the higher energies are from Ref. 9. A comparison of Fig. 12(a) with either Fig. 12(b) or Fig. 12(c) indicates that not all of the Δ_1 symmetry bands contribute to the normal-emission spectra.

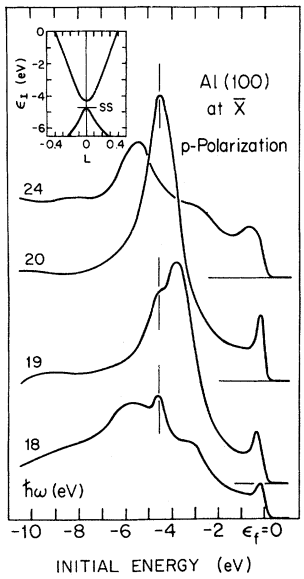

FIG. 16. Photoelectron spectra at various photon energies for $k_{||} = \bar{X}$ (see Fig. 2). The line shows the fixed-energy surface state (SS). The band structure (Ref. 35) along the rod defined by $k_{||} = \bar{X}$ is shown as an inset.

This is due, in part, to the directionality of propagation of the Bloch waves, which is obvious when we write the final state as a sum of plane waves

$$\psi_{n,\vec{k}}(\vec{r}) = e^{i\vec{k}\cdot\vec{r}} \sum_G C_G^{(n)}(\vec{k}) e^{i\vec{G}\cdot\vec{r}} . \quad (6)$$

$\vec{k}$ is the reduced-zone crystal momentum, n is the band index, and the G's are bulk reciprocal-lattice vectors. Equation (6) is particularly useful for discussing the photoemission process, since it relates the reduced-zone to the extended-zone scheme, which is the natural reference system for the photoemission final state. The partial wave

$$e^{i(\vec{k}+\vec{G})\cdot\vec{r}}$$

is a plane wave propagating in the $\vec{k}+\vec{G}$ direction and its amplitude is given by the coefficient $C_G^{(n)}(\vec{k})$.

Consider first the empty-lattice final-band structure shown in Fig. 12(b). If the initial state characterized by $\vec{k} = (0,0,k_z)$ $(0 \le k_z \le 1$ in units of $2\pi/a)$ is excited into the final band associated with the reciprocal-lattice vector (0,0, + 2), then the extended zone K is $(0,0,k_z+1)$, which comes out of the crystal in the normal direction. But if the excitation is to the final band formed by any of the reciprocal-lattice vectors $(\pm1,\pm1,+1)$ then the extended zone k is $(\pm1,\pm1,k_z+1)$. This wave comes out of the crystal with $k_{||} = (\pm1,\pm1)$ which is the $\bar{\Gamma}$ point in the second surface Brillouin zone (see Fig. 11). This excitation will not be seen in normal emission. When the excitation is to a final band with a $(\pm2,0,0)$ or $(0,\pm2,0)$ reciprocal-lattice vector the emission is at $\bar{\Gamma}$ in the third surface Brillouin zone.

When the periodic crystal potential is turned on the bands of Δ_1 symmetry will hybridize and mix so that each band will be associated with several G's. The normal-emission intensity of any direct transition will be determined by the amplitude of the plane-wave components associated with G's of the form $(0,0,2m)$, i.e., $C^{(n)}_{0,0,2m}(k)$ where m is an integer. The bottom two bands in Fig. 12(c) present the simplest illustration of this effect. The two empty-lattice bands associated with G's of the form $(0,0,-2)$ and $(\pm1,\pm1,-1)$ have hybridized. The portion of the band b in Fig. 12(c) labeled b_1 is still primarily associated with the reciprocal-lattice vector (0,0,2) while the b_2 part of this band is primarily of the form $(\pm1,\pm1,-1)$. Likewise, the C_1 part of band C is associated with $G(\pm1,\pm1,-1)$ while C_2 is of the form $G(0,0,-2)$. Therefore, if we would follow a direct transition in normal emission along the band b, the intensity could be large for transitions near X, but would go to zero as the transition moves to Γ in the reduced-zone scheme. The intensity of this transition from the initial band at Γ to the b_2 band would come out at the second zone

center [$\Gamma(2)$].

The discussion above has ignored the problem of matching the bulk Bloch states with plane waves in the vacuum. This matching introduces two new effects. It is possible that an internal partial wave propagating in the direction of detection is reflected from the surface or it is also possible that an internal wave propagating in the wrong direction is elastically scattered at the surface via an umklapp process into the correct direction. In principle, the coupling of a given Δ_1 final band in the bulk to a plane wave in the vacuum can be calculated using a standard LEED calculation, since the photoemission final state is related to a time-reversed LEED state. Such a calculation has been reported for Al(100) by Jepsen *et al.*,[32] where they determined for each energy the transmitted flux into the different final bands from an incident plane wave normal to the surface (no realistic surface potential was included, however). In Fig. 12(c) we show by the heavy lines the parts of each final band which carries more than 50% of the incoming flux. Every Δ_1 band transmits some flux, but this can be as low as 5% for portions of the bands like $c\,1$, $b\,2$, $f\,2$, $g\,1$, $g\,3$, and $h\,1$.

From this calculation[32] we find that in general one part of a band carries most of the flux, and as we see from Fig. 12(c), these parts taken together follow a broken-up free-electron band given by $\vec{G}=(0,0,\pm 2)$ ($m^*\sim 1.09m$ is this calculation, which is based on the Snow potential[32]). The same behavior has been observed for the complicated final-state band structure in GaAs.[29(c)] Although the present calculation extends only to ~ 60 eV above E_f, it is obvious from the shape of the final bands in Fig. 12(c) that the matching conditions are similar at higher energies.

The calculations we have considered so far do not include any damping in the final state (no imaginary part in the potential), as occurs in a real crystal. The inclusion of an absorptive term has important consequences on the observable band structure.[41–43] Every k_z acquires an imaginary part and the classification in terms of evanescent gap states and undamped band states is washed out. Model calculations[41,43] show that the bands associated with the real part of the complex $\vec{k}$ vector can deviate significantly from the band structure without absorption: the magnitude of band gaps is reduced by tails that extend into the gap, small gaps are removed (the bands across the gaps are derived from the real lines in the gap without absorption), and the overall band structure for these damped Bloch waves is bent back towards that of a free electron. (This, however, does not imply that the wave functions should become more like plane waves.) We find that the experimentally determined bands shown in Fig. 12 agree with this picture for energies $\gtrsim 35$ eV above E_f.

It is interesting to note that the experimental bands above 40 eV are reasonably well described by an effective-mass band of $m^*=1.0m$, whereas the calculation indicates $m^*\sim 1.09m$. In the Γ-X direction we observe a small deviation from the free-electron band in the energy range 45–55 eV above E_f, which might be a remnant of the zero-absorption band structure ($f\,1$, $g\,2$, and $h\,2$ bands). The neglect of such non-free-electron effects in a semi-empirical final-state model[7,29(d)] will, of course, be projected back on the initial state.

In the normal-emission geometry, the photoemission properties are complicated for final-state energies $\lesssim 35$ eV. This is caused in part by the large final-state gap at Γ, which is not smeared out in the complex band structure and by the poor coupling condition of the final bands between 20 and 36 eV with a plane wave in the vacuum. From Fig. 17 we see that the intensity of the direct transitions dies away very fast as we approach or penetrate the gap, where the final state is a more strongly damped evanescent wave. The intensity decrease for initial-state energies $\gtrsim -6$ eV in Fig. 17 is attributed to an intensity borrowing by the surface state, which resonates as the direct transitions approach X (Figs. 4 and 11). A similar behavior is observed for the Λ_1 surface state on Cu(111),[31] but is not found for the same surface state on the hexagonal Zn(0001)

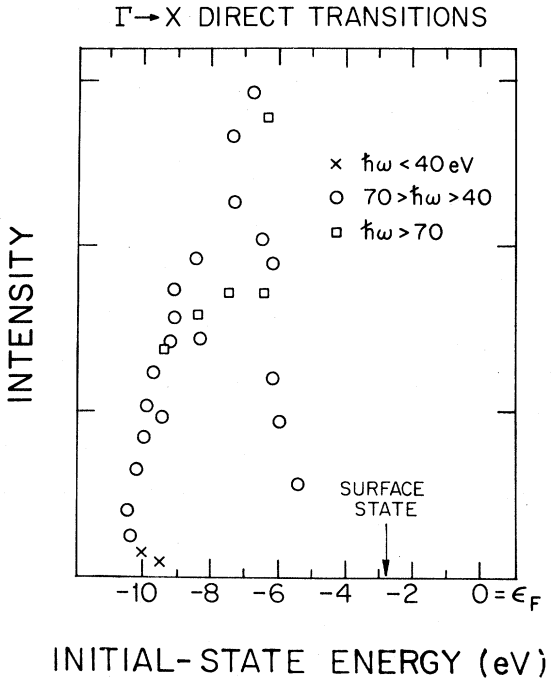

FIG. 17. Intensity of direct transitions in normal emission as a function of the initial-state energy.

surface.[29d] At Γ the only dipole-allowed final state is the p-like Γ_{15} point, which, however, couples very badly to the vacuum plane wave, as Fig. 12(c) shows. For photon energies $\hbar\omega < 40$ eV we observe two weak direct-transition peaks in the spectrum, where the second peak (open circles in Fig. 5) has typically 20—30 % of the intensity of the main peak. Figure 18 shows several normal-emission spectra in the photon energy range of 30—45 eV. For $\hbar\omega < 30$ eV we cannot resolve any direct transition. Between 35 and 40 eV two direct-transition peaks appear, with the weak transition disappearing for $\hbar\omega > 40$ eV. The intense peaks have their origin either from band-gap emission or a weak coupling to the bands d or e near Γ, while the weaker features at ~ 7 eV binding energy correspond to secondary cone emission with an associated G of the form $(0,\pm 2,0)$ or $(\pm 2,0,0)$. Note that the data points agree with the calculated dispersion of the band d, but not the band e. The calculation by Hoffstein and Boudreaux[9] produces better agreement with the data.

A decomposition of the bands $b1, c2$ and the occupied bands in terms of different angular momentum components[38] makes clear why no direct transitions are observed in normal emission for $\hbar\omega \lesssim 30$ eV. Near Γ the initial state is mainly s-like, whereas the only final state that can couple to the outside world, is dominantly d-like. As $\vec{k}$ moves towards X, the initial state acquires more and more p character

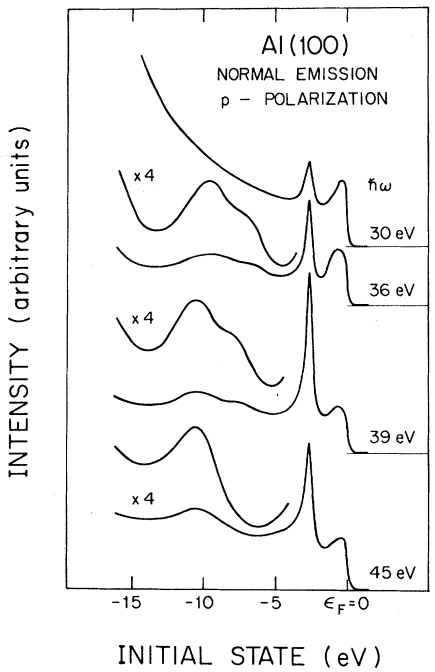

FIG. 18. Normal-emission photoelectron spectra for transitions near the Γ point.

and so does the final state, making dipole-allowed transitions very weak. The situation is different for other directions in $\vec{k}$ space, where direct transitions can be observed at lower photon energies, as, e.g., along the Z axis (see Fig. 6).

B. Non-normal emission: X to W

The off-normal collection geometry ($k_{||} = \bar{M}$) samples states along the z axis of the bulk Brillouin zone, i.e., from X to W in Fig. 2. In this direction the behavior of the final bands can qualitatively be explained with the same arguments presented for the Δ axis in the preceding section. There is, however, one distinct difference: The symmetry is much lower in the off-normal geometry than for normal emission. The point-group symmetry of normal emission is C_{4v} while the z axis has C_{2v} symmetry. When the position of the detector is fixed at $\bar{M}$, the allowed symmetry of the final band is restricted to those that are even with respect to this mirror plane defined by the surface normal and $\bar{M}$. Table II lists the symmetry of all of the different Z bands for a reduced-zone wave vector of the form $k = (0,1,k_z)$, $0 \le k_z \le \frac{1}{2}$, i.e., the $\bar{M}_1$ point of the surface Brillouin zone shown in Fig. 2.

In Fig. 14(b) we have plotted the empty-lattice band structure along the z axis in the reduced-zone scheme appropriate for the $\bar{M}_1$ point. The reciprocal-lattice vectors associated with each back-folded band are indicated. Each band of Fig. 14(b) is at least doubly degenerate, as indicated by the band labeling. The crystal potential splits the degenerate bands as can be seen in Fig. 14(c). We will base the following qualitative discussion on the assumption that the leading term in a plane-wave decomposition of the actual final state is still given by the same G vectors as for the empty-lattice bands. Contributions from other G's are to be expected if a band with the correct symmetry lies nearby in energy. Note that there is always a symmetry change at the W point, such that Z_3 goes to Z_4 or

TABLE II. Symmetry operation. The symmetries of states with reduced-zone wave vector $k = (2\pi/a)(0,1,k_z)$. E is the identity operation, C_2 is a 180° rotation about the z axis, and σ_{xz} and σ_{yz} are reflections through the xz and yz mirror planes, respectively. 1 and -1 denote even or odd symmetry with respect to the given symmetry operation (Ref. 44).

State	E	C_2	σ_{yz}	σ_{xz}
Z_1	1	1	1	1
Z_2	1	1	-1	-1
Z_3	1	-1	1	-1
Z_4	1	-1	-1	1

vice versa. States of Z_3 (Z_4) are even (odd) under a reflection about the yz mirror plane and odd (even) with respect to the xz plane, whereas the irreducible representation Z_1 has the full C_{2v} symmetry.[44] The symmetry change $Z_3 \leftrightarrow Z_4$ at W corresponds to the fact that the extended final state $\bar{k}_i + \bar{G}$ jumps from one z axis to the other nonequivalent z axis (e.g., $\bar{M}_1 \rightarrow \bar{M}_2$), thereby changing the emission direction.

The effects of the symmetry change at W can be illustrated by considering photoexcitation in the reduced-zone scheme plotted in Fig. 14(b). Assume that the initial state is $\vec{k}=(0,1,k_z)$ along the z axis that crosses the surface Brillouin zone at $\bar{M}_1$ in Fig. 2. Excitation from this band into the second band characterized by G's of the form $(\pm 1,-1,-1)$ produces an extended zone $K=(\pm 1,0,-1+k_z)$ or $K=(\pm 1,0,1,+k_z)$ for $(-\frac{1}{2} \leq k_z \leq 0)$. This is a wave which will emerge from the surface Brillouin zone at $\bar{M}_2$ or $\bar{M}_4$ of Fig. 2. The third band of Fig. 14(b) produces an extended zone $K=(\pm 1,0,1+k_z)$ which is also a wave emitted at $\bar{M}_2$ or $\bar{M}_4$. The fourth band changes symmetry ($Z_4 \rightarrow Z_3$) and is associated with $G=(0,0,-2)$ or $(0,-2,-2)$ which gives an extended zone $K=(0,\pm 1,-2+k_z)$. This wave is again emitted from $\bar{M}_1$ or $\bar{M}_3$.

The crystal potential splits the Z_1Z_3 or Z_1Z_4 bands by 1.5 to 2 eV in the lower unoccupied bands. The calculation of Szmulowicz and Segall[6(a)] is plotted in Fig. 14(c). Since each band has a specific symmetry as listed in Table II, the photoionization matrix element $\langle \psi_i \mid \vec{A}\cdot\vec{P} \mid \psi_f \rangle$ can be used to compile a table of the allowed final states for specific initial states (ψ_i) and polarization directions (Table III). If the detector is at $\vec{k}_{\parallel}=\bar{M}_1$ in Fig. 2, then s-polarized light is called odd if $\vec{A}=\vec{A}_x$ and even if $\vec{A}=\vec{A}_y$. This table shows that by using the different polarizations we can, as an example, couple the Z_3 initial state to either the Z_1 or Z_3 final bands (the Z_2 band is always odd in a mirror plane). Experimentally, we only find one final band for all polarization geometries. This can be seen clearly in Figs. 6, 14(a), and 13. The reason is that the inclusion of final-state damping brings the two bands back together into an unresolvable single band. This is reasonable since the 2-eV splitting in the two symmetry bands at W is less than the 2.9-eV lifetime broadening seen in the Fermi-energy intensity data at 20 eV above E_F (Figs. 13 and 19). Therefore, we must consider transitions from a specific symmetry initial band to both symmetry final bands.

The most unambiguous test of the symmetry rules in photoemission is to use s-polarized light parallel and perpendicular to the collection plane. For example, consider emission at the $\bar{M}_1$ point of the surface Brillouin zone into the final bands of Fig. 14(b) associated with reciprocal-lattice vectors of the form $G=(0,0,\pm 2)$ or $(0,-2,\pm 2)$. For these bands (Z_1Z_3) the emission is along the z axis through $\bar{M}_1(\bar{M}_3)$. When the s-polarized light is along the y axis (even in Table III) the $Z_1(Z_3)$ initial band can be excited into the $Z_3(Z_1)$ final band. Both final bands are even in the yz plane, indicating that in the even geometry the Z_1 and Z_3 initial-state bands should be observed. When the polarization is flipped to the odd geometry ($\vec{A}$ along the x axis) then $Z_1(Z_3)$ is excited into the $Z_4(Z_2)$ band. These bands are both odd in the yz plane so neither the Z_1 nor Z_3 initial-state bands can be observed in this geometry. Figure 20 shows this type of measurement for three photon energies. In the even geometry photoexcitation from the Z_1 and Z_3 bands are expected and seen, but in the odd geometry, the Z_3 band is seen even though the symmetry arguments given above require that there should be zero intensity for both the Z_1 and Z_3 bands. At $\hbar\omega=20$ eV the intensity of the Z_3 band in the odd geometry is $\sim 40\%$ of that in the even, while it is only $\sim 20\%$ and $\sim 15\%$ at $\hbar\omega=26$ and 40 eV, respectively. We believe that this apparent violation of symmetry is primarily due to a surface umklapp process.[45] The larger intensity (40%) in the odd geometry at $\hbar\omega=20$ eV could be a result of the mixing of G's of the form $(\pm 1,-1,1)$ from the lower band near W into the $(0,0,-2)$ type final band. Basically, the experiment cannot distinguish between admixing of appropriate plane waves and surface umklapp. However, such mixing is expected to be negligible

TABLE III. The optical transitions for Z band states giving the polarization of the light for the transition to be allowed. If a component of the photon field must be polarized perpendicular to the surface, then the requisite polarization is p polarized. Even or odd refer to polarization vectors which are parallel or perpendicular to the crystal mirror plane containing k.

Initial state	Allowed final states	Polarization
Z_1	Z_1	p polarized
	Z_3	s polarized, even
	Z_4	s polarized, odd
Z_2	Z_2	p polarized
Z_3	Z_1	s polarized, even
	Z_2	s polarized, odd
	Z_3	p polarized
Z_4	Z_1	s polarized, odd
	Z_2	s polarized, even
	Z_4	p polarized

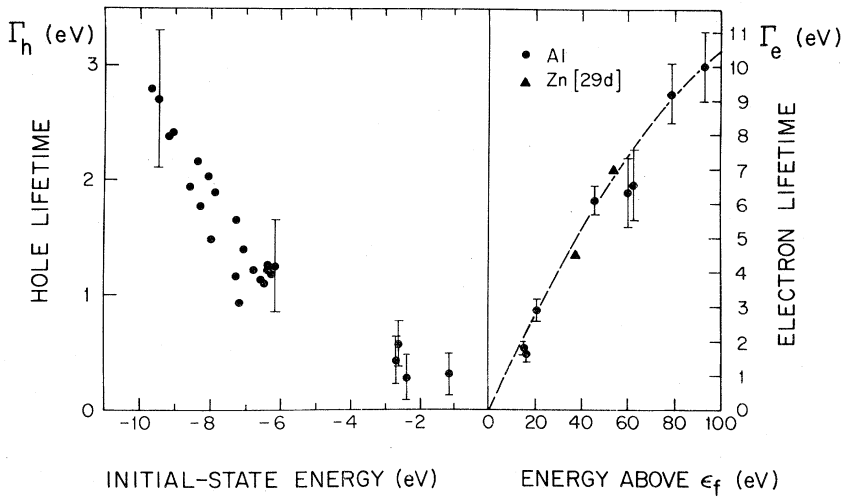

FIG. 19. Electron (Γ_e) and hole (Γ_h) inverse lifetimes as deduced from Fig. 14, the experimental band dispersion, and the width of direct transitions. The data points for Zn are from Ref. 29(d).

near X, yet the Z_3 band is seen there, implying significant contributions from surface umklapp.

The z axis running through $\bar{M}_1(\bar{M}_3)$ and $\bar{M}_2(\bar{M}_4)$ in Fig. 2 has different symmetry properties (in a given coordinate system), but is connected by a surface reciprocal-lattice vector. These surface lattice vectors are not equivalent to any bulk lattice vectors, but instead they are projections of bulk G's of the form $(\pm1,\pm1,\pm1)$, $(\pm1,\pm1,\pm3)$, etc. This means that bulk direct transitions excited along the Z axis through $\bar{M}_2(\bar{M}_4)$ can be scattered via a surface umklapp into the z axis through $\bar{M}_1(\bar{M}_3)$. For example, consider the odd polarization geometry shown in Fig. 20 for collection at $\bar{M}_1$ in the surface Brillouin zone. The direction of the light polarization vector is along the x axis of Fig. 2. This is the even-geometry configuration for collection at $\bar{M}_2(\bar{M}_4)$. Therefore, the $Z_1(Z_3)$ initial band is excited into a $Z_3(Z_1)$ final band at $\bar{M}_2(\bar{M}_4)$. These final states at $\bar{M}_2(\bar{M}_4)$ can be elastically scattered into $\bar{M}_1(\bar{M}_3)$ via a surface umklapp process. If the umklapp process preserves the symmetry of the final band, then the Z_1 final state will be symmetric about the yz plane while the Z_3 band from $\bar{M}_2(\bar{M}_4)$ will be odd at $\bar{M}_1(\bar{M}_3)$. This latter symmetry consideration explains why only the Z_3 initial band is seen in the odd geometry (the intensity of the $Z_1 \rightarrow Z_3$ transition in the odd geometry in Fig. 20 is less than 1% of the emission in the even geometry).

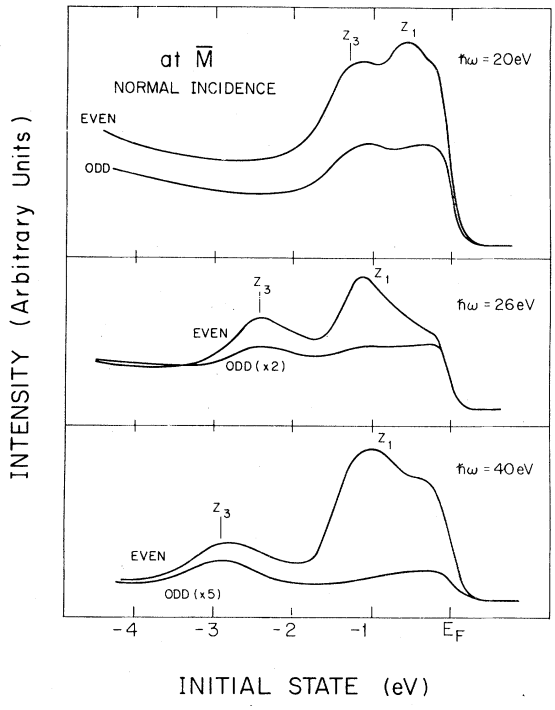

FIG. 20. Spectra at $\bar{M}$ for normal incident light in the odd and even geometry (see text).

Table III can be used to explain the intensity of the Fermi-level crossings shown in the top of Fig. 13. From Fig. 10 we know that the initial bands Z_1 and Z_4 cross the Fermi energy almost at the same k, hence we must ask about transitions from both symmetry bands. In curve b of Fig. 13 the light is s polarized and the collection is perpendicular to the polarization (odd geometry). For $\hbar\omega < 18$ eV the final bands are associated with G's of the form $(\pm1,-1,1)$ so that the initial state must start along the z axis through the $\bar{M}_2(\bar{M}_4)$ point making the polarization even in a coordinate system at $\bar{M}_2(\bar{M}_4)$. Therefore, Table III shows that Z_1 goes to Z_3 and Z_4 to Z_2. For $\hbar\omega > 18$ eV the final bands are asso-

ciated with G's of the form $(0,0,-2)$ or $(0,-2,-2)$, producing emission from an initial state at $\bar{M}_1(\bar{M}_3)$. In this case the only dipole-allowed transitions are $Z_1 \rightarrow Z_4$ and $Z_4 \rightarrow Z_1$. Setting the symmetry considerations produces the following conclusions: (1) there should be no observable transitions for $\hbar\omega < 18$ eV; (2) the only observable transitions above $\hbar\omega \sim 18$ eV is Z_4 to Z_1. This means that the weaker peak in Fig. 13(b) is again due to a surface umklapp process or to band mixing.

Figure 13(a) shows the transition intensity for p-polarized light with the collection perpendicular to the plane of incidence. If the collection is at $\bar{M}_1$ of Fig. 2, then $\vec{A} = (A_x, A_z)$. Table III shows that below $\hbar\omega \sim 18$ eV we could observe $Z_1 \rightarrow Z_1$ while above $\hbar\omega \sim 18$ eV both $Z_1 \rightarrow Z_1$ and $Z_4 \rightarrow Z_1$ can be seen. The sum of both of these two allowed transitions at $\hbar\omega \sim 20$ eV makes the intensity $\sim$ six times larger than the intensity in Fig. 13(b). Our arguments predict an allowed $Z_1 \rightarrow Z_1$ transition at $\hbar\omega \sim 15$ eV which, however, is not observed, presumably due to a small matrix element.

A unique feature of our data at $\bar{M}$ is the large (6–8)-eV wide gap at X centered at ~ 35 eV above E_f [Fig. 14(a)]. This gap is the sum of two different gaps, as the comparison with Fig. 14(c) shows. The lower gap arises from a downward shift of the d-like states from their free-electron value at ~ 35 eV.[6(a)] The bottom of the lower gap is therefore mainly d-like, while the states at the top are predominantly f-like.[38] This gap has been identified by x-ray absorption measurements.[37] The upper gap is caused by the hybridization of the various Z_1 or Z_3 states and is solely a symmetry gap. The flat mainly f-like bands at ~ 34 eV above E_f are not observed in our experiments due to their small perpendicular $\vec{K}$ component and a presumably weak optical transition strength. Only in the vicinity of the X point might the mixing with G's of the type $(0,0,\pm 2)$ or $(0,-2,\pm 2)$ be large enough to allow some coupling to vacuum plane waves. Both gaps together represent an apparent gap with a calculated width of ~ 13 eV.[6(a),38] In the presence of the final-state damping, this width is reduced by tails extending into the gap region, as is obvious from the data in Fig. 14(a). The intensity of the direct transitions decreases as the final state penetrates this gap at X. Transitions from the Z_1 band at the X_1 point, as an example, are not significantly broader in the gap and their intensity is $\geq 30\%$ of the intensity near the gap "edge," indicating that these evanescent gap states penetrate an appreciable distance into the crystal.

An interesting result is obtained for the final-state energies of 55–70 eV. From the extended-zone picture (Fig. 9 in Ref. 8) we would expect at these high energies that the final states follow the solid line $Z_1 Z_4$ up to 80 eV, but Fig. 14(a) and Fig. 14(b) show that they instead follow the $Z_1 Z_2 Z_3 Z_4$ free-electron bands, which are folded back by $\vec{G}$'s of the form $(\pm 2,0,-2)$ and $(\pm 2,-2,-2)$. Dipole selection rules allow the excitation of $Z_3 \rightarrow Z_3$ by the perpendicular and $Z_3 \rightarrow Z_1$ by the parallel component of the $\vec{A}$ vector, respectively. Usually the perpendicular $\vec{A}$ component yields the strongest photoemission peaks [see, e.g., Figs. 13(a) and 13(b)] and hence transitions to the Z_3 final band are expected to be observed for the non-normal incidence measurements. The Z_4 or Z_2 states will not be observed since $Z_3 \rightarrow Z_4$ is a dipole-forbidden excitation and Z_2 states are odd with respect to both mirror planes. Transitions to both Z_1 bands, however, are symmetry allowed and both bands might be seen at least with normal incident light. None of the two empty-lattice bands has the right propagation direction to reach the detector and a detailed calculation would be needed to understand the coupling conditions. Moreover, it is possible that the optical transition strength for these two final bands (or the actual final bands with damping) are sufficiently different to obscure the observation of one of them.

V. LIFETIMES

An estimate of the initial- and final-state lifetimes will be given in this section. The energy broadening caused by the finite lifetime of an excited photoelectron can be obtained from the Fermi-level intensity measurements shown in Fig. 13. For initial states close to E_f the hole lifetime broadening Γ_h can be neglected and the full width at half maximum of the resonances seen in Fig. 13 is a direct measure of the electron inverse lifetime Γ_e[7,8]. We shall neglect here the effects introduced by the finite experimental resolution and the varying matrix element along the considered initial-state band and hence obtain rather an upper limit for Γ_e. The neglect of these effects may also lead to errors in determining the accurate energy of a Fermi-level crossing. Furthermore, we assume that the inverse lifetimes $\Gamma_{e,h}$ do not depend significantly on $\vec{k}$ and we use for the analysis of the normal-emission data the same electron lifetimes, as measured mainly in the off-normal geometry. The results are summarized in Fig. 19 for energies up to ~ 95 eV, together with the values for the nearly-free-electron metal Zn, as taken from Ref. 29(d). The origin of the structures at $\hbar\omega \sim 80$ and 93 eV in Fig. 13 is not clear and the corresponding data should be used with care. From the inverse electron lifetime Γ_e an escape depth l can be defined as $l \approx (1/\Gamma_3)\partial\epsilon_f/\partial k$, if the final band dispersion $E_f(\vec{k})$ is known.

The hole lifetime can be estimated if the width of

a direct transition, the dispersion of the initial and final bands, and the electron lifetime are known. The procedure to follow, however, is not unique, but we prefer here to use the formalism given by Chiang *et al.*[29(c)] The measured peak widths for normal emission and binding energies >6 eV range from 3.5—4.5 eV for $\hbar\omega > 50$ eV and from 0.5—1.2 eV in the off-normal measurements at smaller binding energies for $\hbar\omega \approx 17$—96 eV, respectively. The determined inverse hole lifetimes Γ_h are shown in Fig. 19 for binding energies up to ~ 10 eV. The large experimental uncertainty opens up a broad range for speculations about the possible Auger decay mechanism of the hole in the final state. Simple density of states arguments, however, give a poor fit to the data and indicate that matrix-element effects are important.

VI. CONCLUSIONS

Not only is aluminum a textbook example of a nearly-free-electron metal, but quite often it also serves as a test case for a given band-structure calculations scheme. The need for experimental data was, therefore, obvious and the observed discrepancies between experiment and available theories are rather alarming. The observed difference in the overall bandwidth of ~ 0.5 eV can be explained by the neglect of the nonlocal self-energy terms in the calculational schemes. An explanation for the disagreement on the position of the s/d-like critical point X_1 is not obvious and needs further consideration. It might be interesting, although difficult, to study whether a different final-state relaxation for the s/d- and p-like X_1 and X_4' states can account for the observed differences.

The simplicity of the initial-state band structure of aluminum made it possible to obtain a deeper insight in the photoemission final states in a material, where strong deviations from a nearly-free-electron picture are expected. It is shown experimentally that the damping in the photoemission final state leads to a deformation of the zero-absorption band structure back to an apparent free-electron-like dispersion. However, significant deviations from a free-electron-like final state can nevertheless be observed in the present case for energies up to ~ 50 eV above the Fermi level. This indicates that for a general case of band mapping a realistic calculation, which includes damping effects, is needed as a guide to obtain reliable, semi-empirical final states. Furthermore, a Fourier analysis and a decomposition in terms of angular momentum proved to be very helpful to address intensity questions.

ACKNOWLEDGMENTS

We gratefully acknowledge the support of the University of Wisconsin Synchrotron Radiation Center. This work was supported by the National Science Foundation, MRL Program, under Grant No. DMR-7923647. The authors would like to thank Dr. L. Szmulowicz, Dr. J. Callaway, Dr. V. L. Moruzzi, Dr. P. K. Lam, Dr. Z. Levine, and Dr. J. Wilkins for sending us unpublished calculations or details of published results. Discussions with Professor N. W. Ashcroft, Professor J. Wilkins, and Professor P. Soven have been particularly helpful.

---

*Present address: Dept. of Physics, University of California, Berkeley, CA, 94720.

[1]Neil W. Ashcroft and N. David Mermin, *Solid State Physics* (Holt, Rinehart and Winston, New York, 1976).

[2]N. W. Ashcroft, Philos. Mag. 8, 2055 (1963).

[3]N. W. Ashcroft and K. Sturm, Phys. Rev. B 3, 1898 (1971).

[4]J. R. Anderson and S. S. Lane, Phys. Rev. B 2, 298 (1970).

[5](a) S. P. Singhal and J. Callaway, Phys. Rev. B 16, 1744 (1977); (b) J. Callaway and D. G. Laurent, Phys. Lett. 84A, 499 (1981).

[6](a) F. Szmulowicz and B. Segall, Phys. Rev. B 21, 5628 (1980); (b) Phys. Rev. B 24, 892 (1981).

[7]D. E. Eastman and F. J. Himpsel, in *Physics of Transition Metals, 1980,* edited by P. Rhodes (IOP, London, 1981), p. 115, and references therein.

[8]E. W. Plummer and W. Eberhardt, *Advances in Chemical Physics* (Wiley, New York, 1982), Vol. 49, p. 533.

[9]V. Hoffstein and D. S. Boudreaux, Phys. Rev. B 2, 3013 (1970); Phys. Rev. Lett. 25, 512 (1970).

[10]These are nonlocal potential calculations by Z. Levine and P. Soven using the Hamann, Schluter, and Chiang scheme (Ref. 11).

[11]D. R. Hamann, M. Schluter, and C. Chiang, Phys. Rev. Lett. 43, 1494 (1979).

[12]J. A. Nelson and P. J. Bunyan, J. Phys. F 7, 1467 (1977).

[13]V. Heine and I. Abarenkov, Philos. Mag. 9, 451 (1964).

[14]R. W. Shaw, Phys. Rev. 174, 769 (1968).

[15]We have used the Fourier coefficient of the potential used by Anderson and Lane (Ref. 4) ($V_{200}=0.84$ eV, $V_{111}=0.24$ eV, and $E_f=11.8$ eV). Anderson and Lane fit both the second- and third-zone Fermi surface while Ashcroft (Ref. 2) had only third-zone data to fit. Ashcroft's values were $V_{200}=0.76$ eV, $V_{111}=0.24$ eV, and $E_f=11.6$ eV. We neglect the effects introduced by the temperature dependence of the lattice constants (4.032 Å at 4.2 K, 4.0496 Å at 300 K), which change the overall free-electron bandwidth by 0.1 eV between 0 and 300 K.

[16]The fit of an effective-mass band to the data in Fig. 9 was accomplished by fitting the shape of the band and requiring that the integrated density of states give 3 *e*/at.

[17]The paper of Arbman and Von Barth, see Ref. 18, gives a clear description of what is put into the various contributions to the band structure of aluminum.

[18]Gunnar Arbman and Ulf Von Barth, J. Phys. F 5, 1155 (1975).

[19]L. Hedin, Phys. Rev. 139, A796 (1965); L. Hedin and S. Lundqvist, in *Solid State Physics,* edited by F. Seitz and D. Turnbull (Holt, Rinehart, and Winston, New York, 1969), Vol 23, p. 181; L. Hedin and B. I. Lundqvist, J. Phys. C 4, 2064 (1971).

[20]P. Thiry, D. Chandesris, J. Lecante, C. Guillot, R. Pinchaux, and Y. Petroff, Phys. Rev. Lett. 43, 82 (1979).

[21]G. A. Burdick, Phys. Rev. 129, 138 (1963).

[22]J. F. Janak, A. R. Williams, and V. L. Moruzzi, Phys. Rev. B 6, 4367 (1972); 11, 1522 (1975).

[23]See, e.g., R. L. Benbow and D. W. Lynch, Phys. Rev. B 12, 5615 (1975); L. W. Bos and D. W. Lynch, Phys. Rev. Lett. 25, 156 (1970), and references therein.

[24]C. L. Allyn, T. Gustafsson, and E. W. Plummer, Rev. Sci. Instrum. 49, 1197 (1978).

[25]B. P. Tonner, Nucl. Instrum. Methods 172, 133 (1980).

[26]L. R. Canfield, R. G. Johnston, and R. P. Madden, Appl. Opt. 12, 1611 (1973).

[27]H. J. Levinson and E. W. Plummer, Phys. Rev. B 24, 628 (1981).

[28]The amount of residual oxygen was calibrated using the data of W. Eberhardt and F. J. Himpsel, Phys. Rev. Lett. 42, 1375 (1979).

[29](a) J. Stohr, P. S. Wehner, R. S. Williams, G. Apai, and D. A. Shirley, Phys. Rev. B 17, 587 (1978); (b) K. A. Mills, R. F. Davis, S. D. Kevan, G. Thornton, and D. A. Shirley, *ibid.* 22, 581 (1980); (c) T. C. Chiang, J. A. Knapp, M. Aono, and D. E. Eastman, *ibid.* 21, 3513 (1980); (d) F. J. Himpsel, D. E. Eastman, and E. E. Koch, *ibid.* 24, 1687 (1981).

[30]J. A. Knapp, F. J. Himpsel, and D. E. Eastman, Phys. Rev. B 19, 4952 (1979).

[31]S. G. Louie, T. Thiry, R. Pinchaux, Y. Petroff, D. Chandesris, and J. Lecante, Phys. Rev. Lett. 44, 549 (1980).

[32]D. W. Jepsen, P. M. Marcus, and F. Jona, Phys. Rev. B 5, 3933 (1972).

[33]P. O. Gartland and B. J. Slagsvold, Solid State Commun. 25, 489 (1978).

[34]G. V. Hansson and S. A. Flodstrom, Phys. Rev. B 18, 1562 (1978).

[35]D. Spanjaard, P. W. Jepsen, and P. M. Marcus, Phys. Rev. B 19, 642 (1979).

[36]E. Caruthers, L. Kleinmann, and G. P. Aldredge, Phys. Rev. B 8, 4570 (1973).

[37]C. Senemand and M. T. Costa Lima, J. Phys. Chem. Solids 37, 83 (1976), and references therein.

[38]J. Mueller and J. Wilkins (private communications).

[39]W. Eberhardt and F. J. Himpsel, Phys. Rev. B 21, 5572 (1980); 21, 5650 (1980).

[40]J. Hermanson, Solid State Commun. 22, 9 (1977).

[41]P. B. Pendry, *Low Energy Electron Diffraction* (Academic, London, 1974).

[42]D. W. Jepsen, F. J. Himpsel and D. E. Eastman, Phys. Rev. B 26, 4039 (1982).

[43]P. O. Nilsson and N. Dahlback, Solid State Commun. 29, 303 (1979).

[44]J. C. Slater, *Quantum Theory of Molecules and Solids* (McGraw-Hill, New York, 1965), Vol. 2.

[45]F. J. Himpsel and W. Steinmann, Phys. Rev. B 17, 2537 (1978).